Fabry-Perot microcavity for diamond-based photonics

Erika Janitz, Maximilian Ruf, Mark Dimock, Alexandre Bourassa, Jack Sankey, and Lilian Childress*
Department of Physics, McGill University, Montreal, Canada
(Received 26 August 2015; published 30 October 2015)

Open Fabry-Perot microcavities represent a promising route for achieving a quantum electrodynamics (cavity-QED) platform with diamond-based emitters. In particular, they offer the opportunity to introduce high-purity, minimally fabricated material into a tunable, high quality factor optical resonator. Here, we demonstrate a fiber-based microcavity incorporating a thick ($>10\ \mu$m) diamond membrane with a finesse of 17 000, corresponding to a quality factor $Q \sim 10^6$. Such minimally fabricated thick samples can contain optically stable emitters similar to those found in bulk diamond. We observe modified microcavity spectra in the presence of the membrane, and we develop analytic and numerical models to describe the effect of the membrane on cavity modes, including loss and coupling to higher-order transverse modes. We estimate that a Purcell enhancement of approximately 20 should be possible for emitters within the diamond in this device, and we provide evidence that better diamond surface treatments and mirror coatings could increase this value to 200 in a realistic system.

DOI: 10.1103/PhysRevA.92.043844 PACS number(s): 42.81.Wg, 42.25.Hz, 42.60.Da, 42.50.−p

I. INTRODUCTION

The field of diamond photonics has seen tremendous growth over the past decade [1,2], spurred by new applications of optically active defect centers in metrology [3,4] and quantum information science [5,6]. In particular, the nitrogen-vacancy (NV) defect [7] exhibits long spin coherence times and narrow optical transitions favorable for realizing a solid-state cavity-QED system. In pursuit of this goal, much progress has been made in fabricating low-mode-volume cavities in diamond itself [2,8–10], and Purcell enhancement of the NV zero phonon line as large as 70 has been observed in a diamond photonic crystal cavity [11]. A complementary strategy is to confine the defect in an open Fabry-Perot microcavity [12,13], which provides *in situ* tunability and the possibility for very narrow cavity linewidths. Recently, three groups have observed coupling between an open cavity and an NV center in a nanocrystal [14–17].

A central challenge for diamond photonics is destabilization of defect optical transitions in close proximity to surfaces, especially for defects in nanocrystals or in nanofabricated devices [18]. For example, the aforementioned diamond photonic crystal cavity achieved its high Purcell factor at the expense of spectral diffusion of many GHz [11], far in excess of the near lifetime-limited linewidths of 13 MHz that can be observed in some type IIa samples [19]. While recent advances in surface treatments [20] and fabrication [21] hold promise for realizing optimal NV properties in nanophotonic structures, narrow linewidths are most reliably obtained microns into bulk diamond. The open cavities discussed here can accommodate the larger mode volumes required for such microns-thick samples: both their mode volume V and quality factor Q increase approximately linearly with length, so that the Purcell enhancement F_p depends only on the mirror finesse $\mathcal{F}$ and the ratio of the cavity waist w_0 to the resonant wavelength λ: $F_p \propto \mathcal{F}\lambda^2/w_0^2$ [12]. In addition, their linewidths are comparatively narrow and can be tuned over a wide range *in situ* via the cavity length, potentially allowing exploration of spin-dependent coupling between an NV center and the cavity. Finally, by adjusting the positions of the mirrors, one can optimize the cavity mode spatial overlap with the emitter.

In principle, it is straightforward to incorporate a microns-thick membrane into an open cavity. However, for high finesse $\mathcal{F} > 10^4$ cavities, losses at the 100 ppm level are important. Absorption and scattering must be minimized, and changes in the cavity mode induced by the dielectric interface must be considered. Here, we demonstrate that a fiber-based microcavity can maintain high finesse $\mathcal{F} \sim 17\,000$ (quality factor $Q \sim 10^6$) while incorporating a >10-μm-thick diamond membrane compatible with high-stability defect centers. We further develop a theoretical description for the longitudinal modes (including diffraction effects), and we use perturbation theory to estimate the mixing between transverse modes induced by the membrane. Based on our measurements, we predict our device should be capable of enhancing the NV zero phonon line by a factor of approximately 20.

II. THE FIBER CAVITY DEVICE

We work with a fiber-based Fabry-Perot microcavity [12,13] in a geometry similar to those used to study quantum dots [22] and molecules [23]. The microcavity system [Fig. 1(a)] consists of a concave mirror on the tip of a single mode optical fiber, and a macroscopic flat mirror to which we bond the diamond membrane. Compared with traditional optics, these fiber-based cavities offer advantages in stable alignment and efficient coupling to the single mode propagating in the fiber [12].

The fiber mirror substrate is fabricated using a CO_2 laser ablation process [12]. The ablation laser induces evaporation and melting of the glass on the fiber tip [24], resulting in an approximately Gaussian-shaped dimple [Fig. 1(b)] with an extremely low surface roughness of <0.2 nm rms, as measured with an atomic force microscope. By imaging the fiber core during ablation alignment, we achieve a placement repeatability of 0.5 μm for the ablation spot. The fiber used in our experiments is measured to have a power coupling efficiency to the cavity mode of $\epsilon^2 = 48 \pm 4\%$ (limited by mirror absorption as well as cavity and ablation misalignment; see Appendix A), and an effective radius of curvature $R = 61.0 \pm 1.4\ \mu$m (see Appendix B).

*Corresponding author: lilian.childress@mcgill.ca

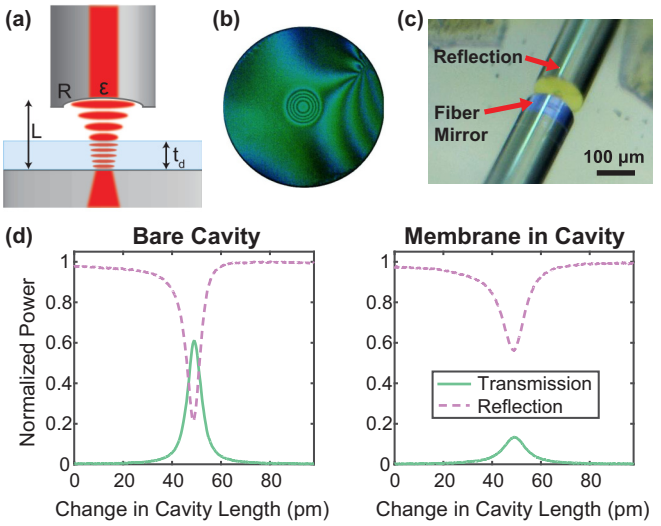

FIG. 1. (Color online) (a) A schematic of the microcavity system illustrating the cavity length (L), mirror radius of curvature (R), diamond membrane thickness (t_d), and coupling efficiency (ϵ) between the fiber and cavity modes. (b) An interferometric image of an ablated fiber, where each subsequent dark fringe corresponds to a change in depth of ≈253 nm. (c) A microscope camera image of the fiber cavity mirror and reflection seen against the diamond membrane. Dark regions in the upper corners are due to partial etching of the mirror beneath the membrane, and some contamination of the diamond surface is also visible. (d) Measured transmission (solid line) and reflection (dashed line) curves for the bare cavity, and membrane-in-cavity configurations, normalized to the peak reflected power. These particular measurements correspond to finesses of $\mathcal{F}_L \approx 37\,000 \pm 1000$ and $\mathcal{F}_L \approx 15\,900 \pm 900$ for the bare cavity and membrane-in-cavity, respectively.

The second mirror substrate is a superpolished macroscopic mirror flat with surface roughness below 0.1 nm rms. The flat and fiber mirrors are coated with a dielectric mirror stack (LASEROPTIK) specified to have a transmission of 70 ± 10 ppm and <24 ppm losses at $\lambda = 637$ nm; the theoretical finesse of the stack design is 53 100. The fiber (stripped of all polymer jacketing) and flat mirrors were both annealed at 300 °C for 5 h under atmospheric conditions to reduce losses in the coatings [25].

The diamond membrane is fabricated from a ⟨100⟩-cut electronic grade single-crystal diamond plate. The bulk diamond was laser cut laterally, producing (20 ± 10)-μm-thick diamond membranes polished to a surface roughness of approximately 5 nm rms. One of the resulting membranes was cleaned in a piranha solution and bonded with Van der Waals forces to a silicon carrier wafer, and approximately 2 μm was etched from the membrane surface using an $ArCl_2$ inductively coupled plasma reactive ion etching (ICP RIE) recipe [26–28]. The etching process reduced the surface roughness to <0.2 nm rms (measured over one optical wavelength squared). The membrane was then removed from the carrier, similarly cleaned in piranha, etched on the other side (again removing 2 μm with $ArCl_2$), and finally bonded to the macroscopic mirror flat. Finally, a third $ArCl_2$ etch was performed to thin the membrane to approximately 10 μm.

To assemble the cavity, the mirror flat is fixed to a tip-tilt mount, while the fiber is clamped to a three-axis manual and piezo stage. The tip-tilt mount enables angular alignment of the cavity mode, while the three-axis stage allows for the study of different regions of the membrane as well as precision control of the cavity length. Figure 1(c) shows an image of the assembled device.

III. EFFECT OF THE MEMBRANE ON CAVITY MODES

A. Cavity finesse

Introducing the membrane into the cavity affects the linewidth of its resonances. To determine the cavity finesse, we scan the position of the fiber mirror while monitoring the cavity's transmission and reflection at a fixed wavelength near 637 nm (provided by a tunable diode laser). In this case, we define the finesse as the ratio of the free spectral range (FSR $\approx\lambda/2$) to the resonance full width at half-maximum (FWHM) measured as a function of the length of the cavity, and we denote it by $\mathcal{F}_L$:

$$\mathcal{F}_L = \frac{\text{FSR in length}}{\text{FWHM in length}}. \quad (1)$$

Note that for the membrane-in-cavity system, this is not necessarily the same as finesse obtained by measuring the resonance spacing and linewidth as a function of laser frequency.

We measure the finesse by first performing a long scan of the cavity length to observe the resonance spacing as a function of the voltage applied to the piezo stage. By scanning the length over about 20 μm (roughly 60 FSR), we can fit the observed resonances to extract the free spectral range and calibrate the piezo stage nonlinearity. Subsequent voltage scans over shorter length ranges (0.6 μm) provide high-resolution data for extracting the cavity linewidth. At each position of interest, we measure 64 transmission and reflection peak data sets to gather statistics on the cavity linewidth. This procedure is followed for all measurements of $\mathcal{F}_L$ presented in Figs. 1–4.

We characterize the transmission and reflection curves for the TEM_{00} fundamental mode using the same fiber mirror for an empty or "bare" cavity, and for a membrane-in-cavity, as illustrated by sample data sets in Fig. 1(d). These measurements are corrected for calibrated losses in the measurement apparatus (outside of the cavity), and they are normalized to the peak reflected power. To determine cavity linewidth, we fit the transmission and reflection data sets to Lorentzian and Fano line shapes, respectively; in practice, the reflection signal gives better signal to noise and was used to calculate cavity finesse. The asymmetric resonances seen in reflection can arise from a slight displacement of the ablation dimple from the fiber core (see Appendix A).

As discussed below, the observed finesse varies with the length of the cavity, the transverse location on the membrane, and the frequency of the laser. At best, we observe a peak finesse of $\mathcal{F}_L \approx 37\,000$ for the bare cavity and $\mathcal{F}_L \approx 17\,000$ for the membrane-in-cavity setup. When we observe different locations on the flat mirror's surface, we find the finesse for the empty cavity typically fluctuates by a few thousand, most likely due to surface contamination or spatially varying

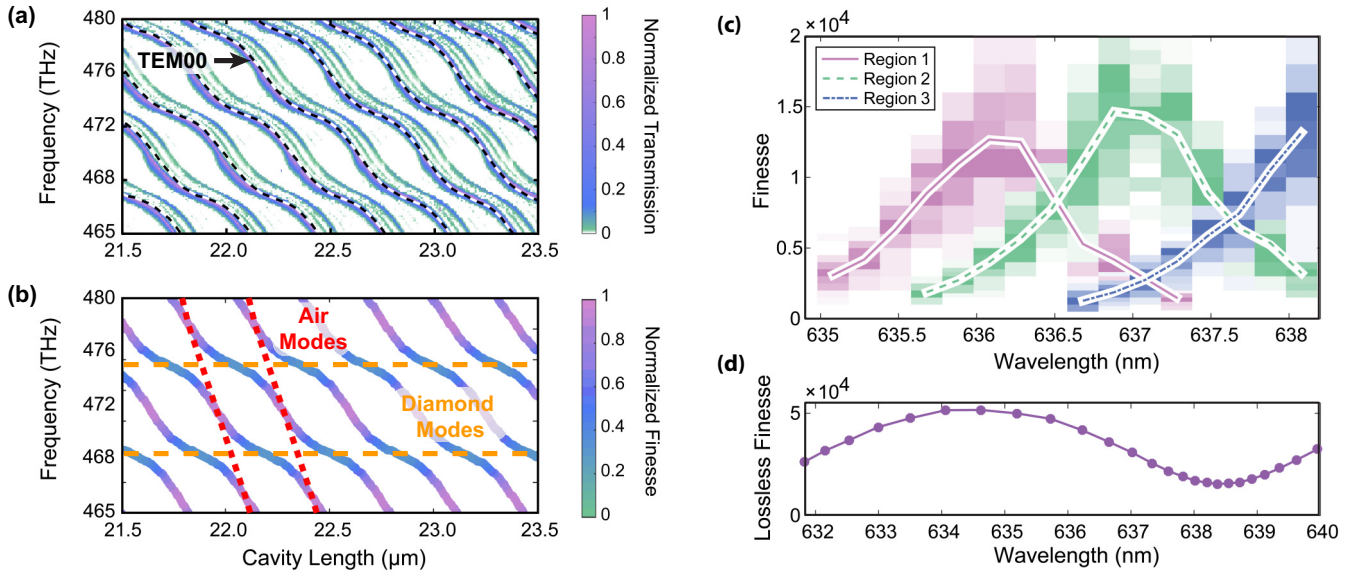

FIG. 2. (Color online) (a) Cavity spectrum obtained by coupling a broadband LED through the flat mirror, and scanning the length of the cavity. An approximate analytic fit [Eq. (3)] to the resonances is overlaid. The error in the x-axis calibration is ± 0.2 μm. (b) A numerical simulation of the normalized finesse $\mathcal{F}_L$ of the cavity resonances including the Guoy phase and mirror stack. Lines indicating the cavity resonances associated with air and diamond regions are overlaid to illustrate the avoided crossings. (c) Finesse vs laser wavelength measured for three different regions of the diamond membrane, corresponding to different membrane thicknesses. The raw finesse data were binned using the Freedman-Diaconis rule [29] to show the underlying distribution, and the binned data are shown through opacity. The mean finesse values are plotted as lines. (d) Simulated finesse vs laser wavelength for a lossless cavity. The absence of scattering losses leads to high finesse over a much larger wavelength range.

surface roughness. With the diamond present, however, the finesse fluctuates by a much larger factor, with no observable cavity resonances in many locations. At first glance, one might presume these fluctuations arise from similar physics, i.e., roughness, contamination, or even crystal defects in the diamond itself. However, as discussed below, such large finesse fluctuations are primarily caused by spatial variations in the diamond layer thickness, which affects the cavity mode structure in an important and predictable way.

B. Mode structure

We characterize the cavity mode structure by illuminating the flat mirror with a broadband LED source, and measuring the spectrum of the light transmitted into the fiber with a grating spectrometer. By gathering data as a function of cavity length, we observe the evolution of multiple longitudinal and transverse modes [see Fig. 2(a)].

The measured white-light spectrum exhibits a canted periodic structure that is markedly different from the behavior of a bare cavity. These features can be quantitatively reproduced by a simple one-dimensional (1D) model. We consider lossless mirrors at each end of the cavity, with a 180° phase shift on reflection (facing the cavity) to approximate the dielectric mirror stack terminated at the high index material (Ta_2O_5 in this case). Between the mirrors are a slab of diamond of thickness t_d and index n_d, and a layer of air with thickness $L - t_d$ and index $n_{\rm air} = 1$ [see Fig. 1(a)]. In the limit of perfect mirrors, the resonant frequencies ν are given by solutions to the transcendental equation,

$$(1 + n_d)\sin\left(\frac{2\pi\nu}{c}[L + t_d(n_d - 1)]\right) = (1 - n_d)\sin\left(\frac{2\pi\nu}{c}[L - t_d(n_d + 1)]\right). \quad (2)$$

Note that while the resonances occur regularly every $c/2\nu$ as the length of the cavity shifts, the variation with frequency is less straightforward. For resonances with a longitudinal mode number much greater than 1, Eq. (2) can be approximated by writing ν in terms of its deviation $\delta\nu$ from an integer multiple m of the average free spectral range, $\nu = \delta\nu + mc/\{2[L + (n_d - 1)t_d]\}$, and neglecting $\delta\nu$ on the right-hand side of Eq. (2) [30], yielding

$$\nu \approx \frac{c}{2\pi[L + (n_d - 1)t_d]}\left\{\pi m - (-1)^m \times \arcsin\left[\frac{n_d - 1}{n_d + 1}\sin\left(\frac{m\pi[L - (n_d + 1)t_d]}{L + (n_d - 1)t_d}\right)\right]\right\}. \quad (3)$$

Fitting Eq. (3) to the fundamental mode frequencies in the cavity spectrum results in an estimated membrane thickness of $t_d = 10.5 \pm 0.2$ μm and the cavity lengths given on the x axis of Fig. 2(a), where the fit results are shown by the dashed lines. Note that we fit resonances over the full 20 μm range of the stage (not shown) to produce these estimates, and we included a cubic nonlinearity in the piezo stage response; the region displayed in the figure is representative of the goodness of fit. The fit deviations arise because the model neglects

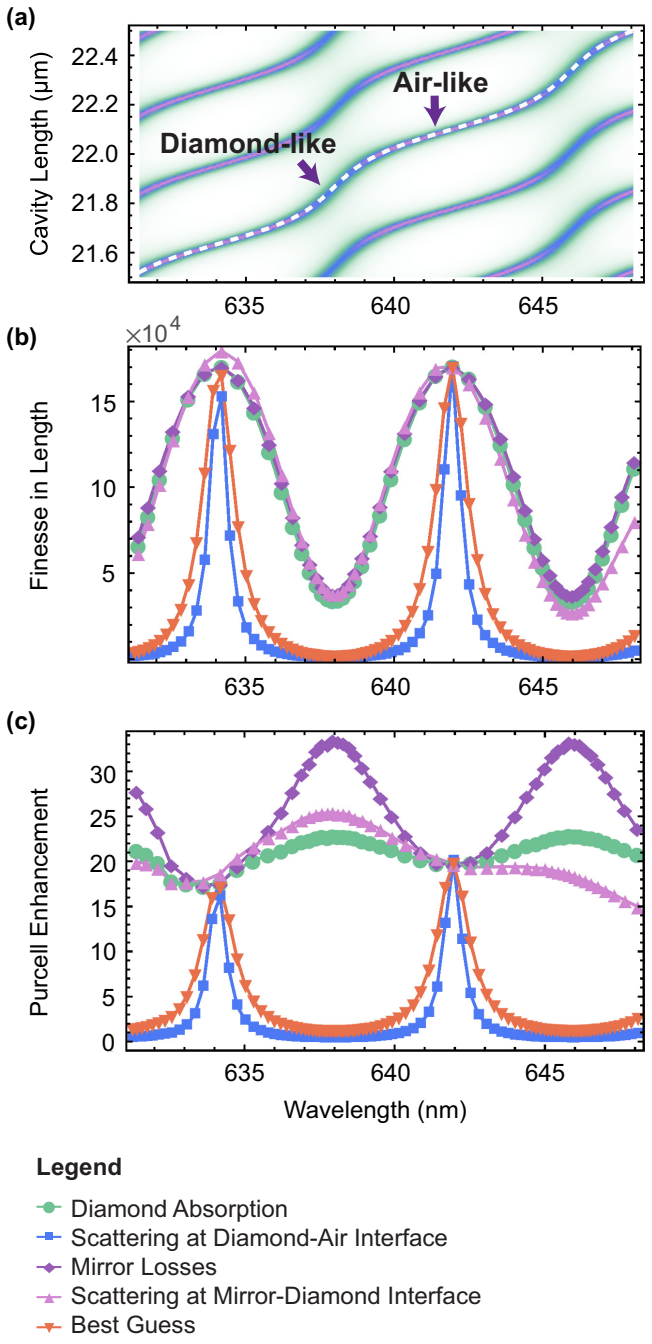

FIG. 3. (Color online) Numerical cavity simulations including wavefront curvature and loss as a function of resonance wavelength. (a) Simulated cavity transmission, illustrating the cavity lengths for which the simulation was performed (dashed line). Steeper-sloped regions correspond to diamondlike modes, while shallower-slopes correspond to airlike modes. (b) Simulated finesse $\mathcal{F}_L$ for different sources of loss in the membrane-in-cavity system. For each simulation, enough loss was added to bring the measured finesse in length down to 17 000. (c) Simulated Purcell enhancement for the same models as in (b). Note that the legend at the bottom applies to both (b) and (c).

the transverse Gaussian field profile and Guoy phase of the cavity mode, which can lead to errors in the estimated length of up to half a FSR ($\lambda/4$) [31]. The fit also allows us to determine the cavity length during transmission and reflection measurements, albeit with an increased uncertainty (roughly $\pm 0.3\ \mu$m) [32].

The model also provides some intuition about the system. If the membrane-air interface were perfectly reflective (i.e., $n_d \to \infty$), it would divide the cavity into two, and the normal modes would separate into "diamond" modes and "air" modes, wherein the field is entirely localized in either the diamond or air, respectively. Since the diamond thickness is fixed, the diamond mode frequencies [horizontal lines in Fig. 2(b)] would not depend on the longitudinal position of the fiber mirror, while the air modes would decrease in frequency as the air gap increases in length [slanted lines in Fig. 2(b)]. Indeed the frequency spacings for these modes would reveal the diamond thickness and cavity length: $\Delta\nu_{\mathrm{di}} = \frac{c}{2n_d t_d}$ and $\Delta\nu_{\mathrm{air}} = \frac{c}{2(L-t_d)}$ for the diamond and air modes, respectively. With finite n_d, these modes are coupled to one another, leading to the large avoided crossings observed in the spectrum; "diamondlike" modes have a shallow slope, while the "airlike" modes have a steeper slope. This behavior is very similar to that of a membrane-in-the-middle system [30], where the air-diamond dielectric interface plays the role of a weakly reflective, vanishingly thin membrane.

Our analysis above focused on the fundamental mode, and indeed, for an ideal spherical ablation dimple, light from the fiber core should couple primarily to the Gaussian TEM_{00} mode. Nevertheless, some higher-order modes are also visible in the spectrum. Similar features observed in the white-light spectrum for the bare cavity are used to extract the effective radius of curvature of the fiber mirror ($R = 61.0 \pm 1.4\ \mu$m), as noted in Sec. II and detailed in Appendix B.

In addition to the analytic 1D model used to find the cavity resonance frequencies, we developed a numerical three-dimensional model for the cavity modes that incorporates wavefront curvature within the cavity and the full dielectric mirror stack. This model includes an approximation that the air-diamond interface follows the curvature of the Gaussian wavefronts, in order to prevent coupling between transverse modes via refraction. Figure 2(b) shows simulated cavity resonances in the absence of any loss, calculated over the same length and frequency range as the white-light transmission data. The cavity parameters used are those extracted from the fit in Fig. 2(a), and full calculation details are provided in Appendix C. The color of each data point shows the calculated value of $\mathcal{F}_L$ normalized to the naive finesse estimate of $\frac{\pi}{T}$, where T is transmission per pass of one mirror, and all other loss processes are neglected. The highest finesse values are obtained when the laser frequency is tuned to an airlike mode, approaching the naive estimate. Conversely, if the laser frequency is tuned to a diamondlike mode, the measured finesse will be consistently lower than expected.

We emphasize that our models thus far assume no losses, meaning the aforementioned finesse fluctuations arise entirely from interference effects. The finesse limitations can be understood by considering the effect of attaching a diamond membrane to the flat mirror. The dielectric coatings used for our mirrors are terminated with a high-index material, and they are optimized for use in air. Diamond has a high index of refraction ($n_d = 2.417$), which effectively lowers the reflectivity of the flat mirror, corresponding to a decrease

in finesse for modes in which the electric field is more confined to the membrane. Quantitatively, the lossless 1D analytic model predicts that the finesse of the diamondlike modes is reduced by a factor of $2/(n_d^2+1) \approx 0.3$. Conversely, if low-index-terminated mirrors were used, the diamondlike modes would exhibit the naive finesse while the airlike modes would have finesse reduced by $2/(1/n_d^2+1) \approx 0.6$.

A central prediction of this calculation is that the mode structure can cause dramatic finesse variations with laser wavelength. Moreover, because the mode structure shifts with t_d, peak finesse values should occur at different frequencies for different membrane thicknesses. Figure 2(c) shows the measured finesse $\mathcal{F}_L$ as a function of laser wavelength for three regions on the diamond membrane with marginally different thicknesses [33]. The square data points correspond to raw finesse data (binned using the Freedman-Diaconis rule [29] to show the underlying distribution) where opacity illustrates measurement frequency. The mean finesse is plotted with a line. For each region, the peak finesse occurs at some wavelength corresponding to an airlike mode. The finesse decreases as the laser is tuned away from this wavelength, and the electric field becomes more localized in the diamond membrane.

While the qualitative features of our data in Fig. 2(c) are similar to the lossless model predictions, the drop in finesse is notably larger and steeper. For comparison, Fig. 2(d) shows the numerically simulated finesse for the ideal lossless system, which exhibits much more gradual variations. As discussed quantitatively below, the discrepancy can only be explained by including loss primarily at the air-diamond interface, such as scattering from roughness or contamination. The sharp wavelength dependence again arises from interferometric effects: when there is an electric field node at the air-diamond interface, field-driven surface losses are strongly suppressed. In this geometry, a node appears at the air-diamond surface only for the airlike mode, providing a mechanism for the sharp finesse peaks in Fig. 2(c).

To quantitatively understand the effects of loss, we add different absorption and scattering mechanisms to the numerical transfer matrix model described in Appendix C. We consider loss in the mirrors, loss caused by scattering at the diamond interfaces, and absorption in the diamond. The mode-mixing mechanisms for loss discussed in Sec. V should be minimal at the short cavity lengths used in Fig. 2(c), and they would not produce the repeatable behavior with wavelength we observe, so we do not consider them here. Loss inside the mirrors and diamond is modeled by adding complex components to the refractive indices of the layers. Scattering by surface roughness of the diamond membrane is added by adjusting the interface reflection and transmission coefficients according to [34,35]

$$r_{ij} = r_{ij}^{(0)} e^{-2(2\pi\sigma n_i/\lambda)^2}, \tag{4}$$

$$t_{ij} = t_{ij}^{(0)} e^{-(1/2)[2\pi\sigma(n_i-n_j)/\lambda]^2}, \tag{5}$$

where r_{ij} (t_{ij}) is the amplitude reflection (transmission) coefficient going from material of index n_i into material of index n_j, σ is the rms surface roughness, λ is the wavelength in vacuum, and $r_{ij}^{(0)}$ and $t_{ij}^{(0)}$ are the lossless Fresnel coefficients. These reflection and transmission coefficients are used in the transfer matrix describing each diamond surface. To quantitatively compare the effects of each individual source of loss, we increase its strength sufficiently to bring the peak finesse $\mathcal{F}_L$ down to our observed value of 17 000 (while holding other sources of loss at zero). We then calculate the cavity modes and linewidths for the cavity parameters extracted from the fit in Fig. 2(a) over the cavity lengths illustrated in Fig. 3(a).

Figure 3(b) shows $\mathcal{F}_L$ as a function of wavelength, as predicted by several loss models. As noted earlier, scattering at the air-diamond interface behaves qualitatively differently from the other loss models, and most closely approaches the features we observe in Fig. 2(c). Because there is always a node at the high-index-terminated mirror surface, scattering from the diamond-mirror interface does not produce such sharp features.

Figure 3(b) also includes simulations using our best estimate for the specific losses in our system. Enough mirror loss was added to bring the finesse down to 37 000 (peak finesse measured for the bare cavity), and we set the diamond-mirror interface roughness to 0.19 nm rms (as measured for similar samples). To match the features in Fig. 2(c), we added sufficient scattering at the air-diamond interface to produce a peak in $\mathcal{F}_L$ [see Fig. 3(b)] with a FWHM of 1.14 nm [the linewidth of the central peak in Fig. 2(c)]. Finally, absorptive loss was added to bring the peak $\mathcal{F}_L$ value down to 17 000. Notably, a very large air-diamond surface roughness ($\sigma = 3.5$ nm rms) was required to reproduce the features of Fig. 2(c). This roughness is far larger than values <0.2 nm rms measured on diamond samples etched by $ArCl_2$, and it indicates that some additional surface scattering or contamination is likely to blame.

After optical measurements were concluded, AFM measurements of the membrane revealed a greater surface roughness than expected. We observed roughness between 0.8 and 23 nm rms in the nominally smooth areas of the membrane, with the majority of measurements around 1 nm rms. The increased roughness was likely caused by the third $ArCl_2$ etch (while bonded to the mirror), which produced noticeable surface damage in some areas of the membrane [see Fig. 1(c)]; the regions used in these experiments appeared unaffected, but in fact they suffered roughening.

The discrepancy between the measured roughness and the model predictions can only be explained by another loss mechanism sensitive to the magnitude of the electric field at the surface of the diamond. Surface absorption (caused, for example, by contamination deposited in the final etch) could provide such a mechanism. Indeed, when we add a thin, lossy, dielectric layer to the diamond-air interface in our model, we see sharp features in the finesse as a function of wavelength similar to those seen from roughness. However, we cannot differentiate between surface roughness and absorption in the finesse features, and roughness must certainly be present whereas surface absorption is merely possible, so we include only surface roughness in the presented calculations. Nevertheless, in either case it is likely that significantly reduced losses could be obtained with better surface preparation. Based on our simulations, a clean surface with state-of-the-art surface roughness $\sigma = 0.19$ nm rms is compatible with finesse $>10^6$ for airlike modes and >50 000 for diamondlike modes.

IV. ESTIMATION OF PURCELL ENHANCEMENT

A figure of merit for cavity systems is the Purcell factor F_p, which describes the spontaneous-emission enhancement of an emitter into the cavity mode. The enhancement depends on the position of the cavity mode maximum relative to the emitter, as well as the orientation of the emitter dipole relative to the mode polarization. The fiber cavity geometry allows considerable optimization of these mode-matching factors: in addition to searching for defects of appropriate depth in the membrane to lie at an antinode, transverse alignment, a slight axial shifting of the wavefronts with cavity length due to Guoy phase effects, and adjustable cavity polarization (via fiber rotation) can all be used to optimize overlap *in situ*. The opportunity to search for defects allows use of as-grown NV centers as well as the selection of emitters with desired properties. Moreover, the dipole axes of an NV center can be controlled with electric fields [36], in principle enabling perfect orientation overlap even for ⟨100⟩ membranes.

To predict the Purcell enhancement that could feasibly be observed in this cavity system, we therefore consider F_p for an optimally located and oriented emitter [37,38],

$$F_p = \frac{3c\lambda^2}{4\pi^2 n_d \Delta\nu} \frac{|E_{\max}|^2}{\iiint n^2(\mathbf{r}) E^2(\mathbf{r}) d\mathbf{r}^3}. \tag{6}$$

Here, $\Delta\nu$ is the cavity linewidth in frequency, λ is the resonant wavelength, $E(\mathbf{r})$ and $n(\mathbf{r})$ are the electric field and index of refraction within the cavity, and $E_{\max}$ is the electric field at the emitter in the diamond, assuming perfect emitter orientation and location. Notably, the Purcell factor depends on the linewidth in frequency, not length. As we are not currently able to directly measure the cavity spatial mode and $\Delta\nu$, we use our model and measurements of $\mathcal{F}_L$ to provide a theoretical estimate of the Purcell enhancement available in this cavity geometry.

In our analytic 1D model, it is straightforward to calculate the mode integrals of Eq. (6) and the linewidth $\Delta\nu$ in terms of the mirror finesse $\mathcal{F}$ (a function of only the lossless mirror reflectivity). This yields a simple result in the limit of large $\mathcal{F}$:

$$F_p^{(A)} = \mathcal{F} \frac{6\lambda^2}{n_d^3 \pi^3 w_0^2}, \tag{7}$$

$$F_p^{(D)} = \mathcal{F} \frac{12\lambda^2}{(n_d^3 + n_d)\pi^3 w_0^2}, \tag{8}$$

where $F_p^{(A)}$ ($F_p^{(D)}$) is the Purcell enhancement for airlike (diamondlike) modes, and w_0 is the $1/e^2$ intensity radius of the cavity waist. Note that in the limit $n_d \to 1$, these match what one would obtain from the standard Purcell formula $(3\lambda^3/4\pi^2)(Q/V)$ with a mode volume of $V = (\pi/4)w_0^2 L$ [37] and $Q = 2L\mathcal{F}/\lambda$.

The two types of modes have different Purcell factors because they have different vacuum electric field maxima in the diamond and different cavity linewidths in frequency. The variation in $\Delta\nu$ has contributions from the reduced reflectivity of the flat mirror (due to the diamond layer) as well as the relative round-trip times of the diamond and air half-cavities. Such effects are similar to finesse oscillations observed in optomechanical systems [39]. Remarkably, in the high finesse limit of the lossless 1D model, the length dependence of the vacuum electric field maximum in diamond precisely cancels the length dependence of $\Delta\nu$, yielding the simple expressions above.

For lossless systems, $\mathcal{F}$ matches the peak value of $\mathcal{F}_L$, and one might be tempted to use Eqs. (7) and (8) with our observed peak finesse and cavity geometry to determine the Purcell enhancement of our device. Such a calculation (using $\mathcal{F} = 17\,000$, $w_0 = 2.2$ μm, and $\lambda = 637$ nm) would predict $F_p^{(A)} \approx 20$ and $F_p^{(D)} \approx 33$. However, adding in loss does not simply reduce $\mathcal{F}$: the location of the loss (in diamond or air) will affect the modes differently, and in general we find that using Eqs. (7) and (8) with $\mathcal{F} = \max(\mathcal{F}_L)$ overestimates the best Purcell enhancement for realistic systems where loss is associated with the diamond.

Figure 3(c) shows the Purcell factor calculated using the numerical model with the different loss mechanisms described in the previous section. While mirror absorption produces similar results to the predictions of Eqs. (7) and (8), qualitatively distinct behavior appears from the surface losses that likely limit our system. In particular, we predict a maximum Purcell enhancement of approximately 20 for our current device geometry. However, our analysis also suggests that significant improvements can be obtained. For example, if surface losses can be limited to the observed roughness after $ArCl_2$ etching (<0.2 nm rms), and higher reflectivity mirror coatings are used, a cavity finesse of 50 000 can be maintained even with an antinode at the air-diamond interface. Using a 30 μm radius-of-curvature mirror (attainable in our laser ablation setup), a 5-μm-thick membrane, and a cavity length of 10 μm, a maximum Purcell factor of around 200 could be reached. Such a cavity would also couple efficiently to the fiber mode (>85% with perfect alignment and low-loss mirrors [40]) and have a linewidth ∼300 MHz, which is large enough to accommodate minor spectral diffusion but small enough to resolve the excited-state structure of the NV center.

V. FINESSE CHANGES WITH CAVITY LENGTH

Beyond the absorption and scattering processes considered above, a thick diamond membrane could also induce an additional, potentially important source of loss, namely mixing between transverse modes of the cavity. Our numerical model has assumed that the air-diamond interface follows the spherical wavefront of the cavity mode, allowing for a description of the cavity eigenstates in terms of two Gaussian beams in the diamond and air regions. The real planar interface, however, deviates from this requirement, and it can thereby couple the TEM_{00} mode into higher-order Hermite-Gaussian modes. Because high-order transverse modes have a larger spatial extent, this mechanism could induce additional losses caused by clipping at the small fiber mirror. This type of loss would behave differently from those discussed previously because it would depend on the length of the cavity, with greater losses expected when higher-order modes approach degeneracy with the fundamental.

To estimate such losses, we apply nondegenerate perturbation theory (see Appendix D) to calculate the first-order eigenstates of the membrane-in-cavity. The fraction of those eigenstates clipped at the fiber mirror can then be calculated to determine the loss per round trip. We begin with zero-order

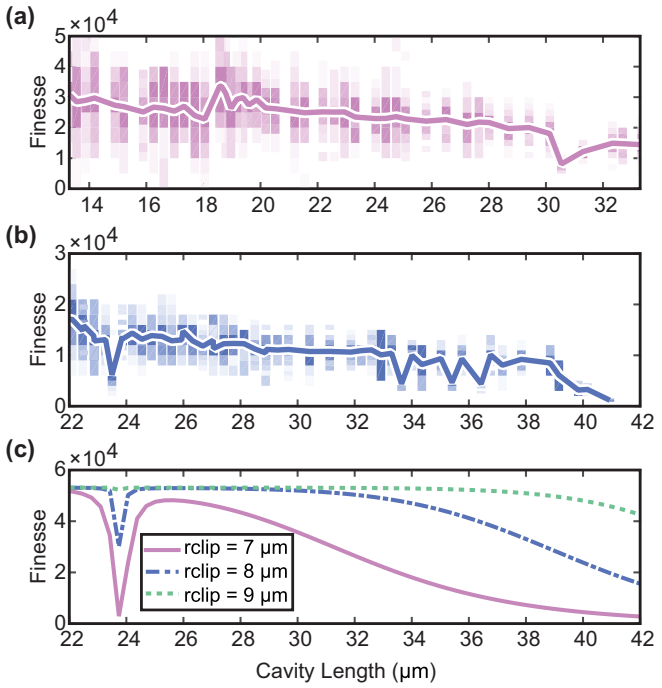

FIG. 4. (Color online) (a) Finesse as a function of length measured for a bare cavity. In (a) and (b), binned raw finesse data are shown through opacity, while the mean finesse as a function of length is indicated by the solid line. (b) Finesse as a function of length measured for a cavity containing a 10.5 μm diamond membrane. The length axis is changed from (a) so that the beam radius on the fiber mirror takes on the same values over the range of collected data. (c) A simulation of finesse as a function of length including perturbative coupling to higher-order modes evaluated for different mirror clipping radii.

modes from the three-dimensional model discussed in Appendix C. We then treat the volume of diamond between the curved, wavefront-matching surface and the true flat interface as the perturbative volume. The first-order correction to the eigenstate is given by [41]

$$\psi^1 = \kappa_{00} \sum_{m\neq 00} \frac{\iiint \psi_m(\mathbf{r})\left(n_d^2 - 1\right)\phi_{00}(\mathbf{r})d\mathbf{r}^3}{\kappa_m - \kappa_{00}}\psi_m, \qquad (9)$$

where the eigenstate is $\psi \approx \phi_{00} + \psi^1$, ϕ_{00} is a TEM_{00} zero-order cavity mode derived from our model, ψ_m is the mth zero-order mode (including all longitudinal and transverse mode numbers), $\kappa_m = (\frac{\omega_m}{c})^2$ contains the eigenfrequency ω_m for the mth mode, and the integral is taken over the volume of the perturbation. The overlap integral couples only even-order transverse modes, and it falls off quickly with transverse mode number. In practice, we have included transverse mode numbers whose sum is $\leqslant 6$. Because the denominator grows quickly as the mode frequencies diverge, we consider corrections only from the two longitudinal modes closest in frequency to ω_{00}.

To examine the importance of these perturbative couplings experimentally, we measured finesse as a function of cavity length with and without the membrane [see Figs. 4(a) and 4(b)]. The bare cavity finesse exhibits a decreasing slope as a function of cavity length, which arises from coupling to lossy higher-order modes caused by the Gaussian shape of the fiber dimple [42,43]. We offset the x axes of the bare cavity and membrane-in-cavity so that the beam radii on the fiber mirror would match, varying from 2.5 to 3.6 μm over the length range presented in Figs. 4(b) and 4(c). For the membrane-in-cavity, in addition to the decreasing slope seen for the bare cavity, we measured intermediate drops in finesse at specific cavity lengths. Since we use the same fiber mirror in both data sets, these dips must be associated with the membrane, and they could be caused by coupling to lossy higher-order transverse modes. For comparison, we simulated the cavity finesse (ignoring all other loss processes) using the first-order correction to the electric field wave function [Eq. (9)] for different clipping radii on the fiber mirror, outside of which all light is assumed to scatter out of the cavity. The result is shown in Fig. 4(c), which exhibits qualitatively similar drops in finesse at certain resonant lengths.

We lack the detailed surface profile data to accurately parametrize our membrane and fiber dimple topography, so the simulations cannot include the exact perturbations present in the measurement (for example, it likely also contains a wedge, which would couple TEM_{00} and TEM_{10} modes). Nevertheless, our calculations demonstrate that the finesse reductions observed at specific cavity lengths in Fig. 4(b) could reasonably be caused by this mechanism. Perhaps more importantly, these data illustrate that perturbative losses are not a major impediment to working with planar membranes, even at relatively large thicknesses >10 μm and over a range of cavity lengths. Furthermore, as the diamond thickness diminishes, the perturbative coupling drops, indicating that it should be a negligible effect for few-micron-thick membranes.

VI. CONCLUSION

We have shown that high finesse $\sim$17 000 can be maintained in a Fabry-Perot microcavity even with incorporation of a thick diamond membrane. The membrane modifies the cavity modes, leading to variations in linewidth for different membrane thicknesses or different resonant frequencies. Our simulations indicate that surface losses dominate, producing qualitatively different behavior from bulk absorption. Membrane-induced coupling to higher-order transverse modes, conversely, does not greatly impact device performance. We anticipate that, despite the large surface losses, the current cavity will allow about a 20-fold Purcell enhancement for diamond-based emitters, which in the case of the NV center would direct more than a third of its emission into the zero phonon line. Furthermore, device performance in this case is limited by surface roughness or contamination that is well above the currently attainable limits [27,28].

When cooled to cryogenic temperatures and locked to the NV resonance frequency, such devices could significantly enhance the efficiency of photon-mediated entanglement between distant defects [44]. Moreover, the cavity linewidth is below the typical spacing between spin-resolved resonant optical transitions in the NV center, enabling exploration of spin-dependent cavity effects. With improved diamond surface treatment and higher reflectivity mirrors, finesse $\sim 10^5$ should be possible [12], and shorter cavities with smaller

radius-of-curvature mirrors could enhance the cavity cooperativity by another order of magnitude [17]; even with current fabrication capabilities, Purcell enhancements in the range of 200 appear within reach. Ultimately, this highly tunable open-cavity geometry could offer a route toward an efficient or even deterministic interface between single photons and solid-state spins.

ACKNOWLEDGMENTS

We acknowledge support from NSERC, FRQNT, the Canada Foundation for Innovation, Canada Research Chairs, and INTRIQ. We also thank Tina Muller, Marie-Josée Gour and Florian Leroy for assistance in developing diamond fabrication recipes at the Institut Interdisciplinaire d'Innovation Technologique (3IT), and we acknowledge CMC Microsystems for fabrication support through the MNT Finanical Assistance program.

APPENDIX A: ESTIMATION OF BARE CAVITY PARAMETERS

The following section describes a method for extracting some parameters of the bare fiber cavity system given measurable quantities and a one-dimensional model shown in Fig. 5. These calculations permit us to understand the asymmetric line shapes observed for both the bare and membrane-in-cavity systems.

In this model, the mirrors have real amplitude transmission and reflection coefficients t and r, and we account for a loss per round trip in the cavity of $1-e^{-2\alpha}\approx 2\alpha$. Assuming that light is launched into the cavity through the fiber, $E_{\rm in}$ is the incident electric field, $E^0_{\rm ref}$ is the reflected field that is coupled back into the fiber core, $E'_{\rm ref}$ is the reflected field that is not coupled into the fiber core, and $E_{\rm trans}$ is the field coupled to the (free space) transmitted mode. The field circulating within the cavity is represented by $E_{\rm circ}$, which is defined just to the right of the left-hand mirror; the change in amplitude and phase incurred in one round trip is represented by the round trip gain: $g_{\rm rt}=e^{-2\alpha}e^{-\frac{2iL\omega}{c}}$. We consider imperfect cavity coupling, where ϵ_1 is the overlap between the fiber and cavity modes, and ϵ_2 is the coupling coefficient between the cavity and transmitted modes (for our analysis, we set $\epsilon_2\approx 1$). If the ablation spot is not perfectly centered on the fiber core, the promptly reflected light that is coupled back into the fiber mode can be described by a complex coupling coefficient η, which has a magnitude less than unity as well as a nonzero phase for imperfect alignment. The relevant relationships between these parameters are given by

$$E^0_{\rm ref}=-e^{-2\alpha-\frac{2iL\omega}{c}}rt\epsilon_1E_{\rm circ}+r\eta E_{\rm in}, \tag{A1}$$

$$E_{\rm circ}=e^{-2\alpha-\frac{2iL\omega}{c}}r^2E_{\rm circ}+t\epsilon_1E_{\rm in}, \tag{A2}$$

$$E_{\rm trans}=e^{-\alpha-\frac{iL\omega}{c}}t\epsilon_2E_{\rm circ}. \tag{A3}$$

Solving for the transmitted and reflected powers ($|E_{\rm trans}|^2$ and $|E^0_{\rm ref}|^2$), normalized to the input power ($|E_{\rm in}|^2$), yields the power reflected (P_r) and transmitted (P_t):

$$P_r=\frac{r^2\left|\left[t^2\epsilon_1^2+\left(-e^{2\alpha+\frac{2iL\omega}{c}}+r^2\right)\eta\right]\right|^2}{e^{4\alpha}+r^4-2e^{2\alpha}r^2\cos\left[\frac{2L\omega}{c}\right]}, \tag{A4}$$

$$P_t=\frac{e^{2\alpha}t^4\epsilon_1^2\epsilon_2^2}{e^{4\alpha}+r^4-2e^{2\alpha}r^2\cos\left[\frac{2L\omega}{c}\right]}. \tag{A5}$$

We set $\eta=a+ib$ and expand the cosine terms to second order in ΔL, where $L=m\lambda/2+\Delta L$ and m is an integer, resulting in power line shapes of the form

$$P_r=\frac{(a_1+a_2\,\Delta L)}{\pi}\frac{\left(\frac{\delta L}{2}\right)^2}{\left(\frac{\delta L}{2}\right)^2+\Delta L^2}+y_0, \tag{A6}$$

$$P_t=\frac{a_3}{\pi}\frac{\left(\frac{\delta L}{2}\right)^2}{\left(\frac{\delta L}{2}\right)^2+\Delta L^2}, \tag{A7}$$

where δL is the FWHM cavity linewidth measured in length, and

$$y_0=(a^2+b^2)r^2+at^2\epsilon_1^2, \tag{A8}$$

$$a_1=\pi t^2\epsilon_1^2\frac{a(r^4-e^{4\alpha})+r^2t^2\epsilon_1^2}{(e^{2\alpha}-r^2)^2}, \tag{A9}$$

$$a_2=\frac{4\pi b\,e^{2\alpha}r^2t^2\epsilon_1^2\omega}{c(e^{2\alpha}-r^2)^2}, \tag{A10}$$

$$a_3=\pi\frac{e^{2\alpha}t^4\epsilon_1^2\epsilon_2^2}{(e^{2\alpha}-r^2)^2}. \tag{A11}$$

Note that this produces a Fano line shape in reflection. The parameters $\{y_0,a_1,a_2,a_3\}$ can be extracted from our data by fitting the transmission and reflection curves and calibrating the input power. In addition, we use measurements of the finesse $\mathcal{F}$ and the following relationships to fully constrain the cavity parameters:

$$\mathcal{F}=\frac{\pi}{\alpha+t^2}, \tag{A12}$$

$$t^2+r^2+\alpha=1, \tag{A13}$$

as well as the known laser frequency ω and $\epsilon_2=1$. With these expressions, one can solve for all of the cavity parameters of

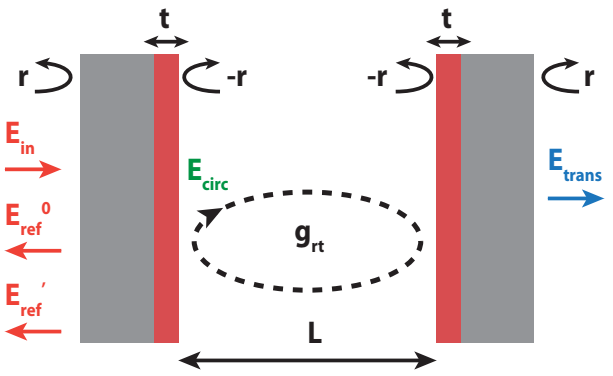

FIG. 5. (Color online) The one-dimensional model used to estimate bare cavity parameters. L is the cavity length, r and t are the mirror amplitude reflection and transmission coefficients, $g_{\rm rt}$ is the round-trip gain of the cavity, and $E_{\rm in}$, $E^0_{\rm ref}$, $E'_{\rm ref}$, $E_{\rm trans}$, and $E_{\rm circ}$ are the electric fields at the input, reflected into the fiber, reflected into other modes, transmitted, and circulating in the cavity, respectively.

interest. For example, using data acquired in a bare cavity of length 12.2 ± 0.3 μm, and expanding in α to first order about zero, we obtain

$$t = (8.8 \pm 0.2) \times 10^{-3},$$
$$r = -0.999\,957 \pm 0.000\,001,$$
$$a = 0.61 \pm 0.02,$$
$$b = 0.14 \pm 0.04,$$
$$\epsilon_1 = 0.69 \pm 0.03,$$
$$\alpha = 8 \pm 1 \text{ ppm}.$$

This yields a power transmittance of $T = 78 \pm 3$ ppm, which agrees with the quoted coating value of $T = 70 \pm 10$ ppm. The combined absorption and scattering losses were quoted to be <24 ppm, which also agrees with the derived α value.

Note added: While in the final stages of preparing this paper, we became aware of detailed theoretical and experimental exploration of the origin of asymmetric line shapes associated with misalignment of fiber cavities [45,46].

APPENDIX B: CALCULATING THE EFFECTIVE RADIUS OF CURVATURE

The Gaussian-shaped ablation dimple can be approximated by a parabola near the center, which has a well-defined radius of curvature. This radius is appropriate for cavity modes with small beam diameters on the mirror. As the cavity length is increased, the mode diameter grows and the approximation breaks down. In this regime, it is more accurate to estimate the effective mirror radius from the spacing of the higher-order TEM modes. If $\Delta\nu_{\text{trans}}$ is the difference in frequency between adjacent transverse modes with the same longitudinal mode (e.g., $\text{TEM}_{m,n}$ and $\text{TEM}_{m,n+1}$), the effective radius of curvature is

$$R = L\left[1 - \cos^2\left(\frac{\Delta\nu_{\text{trans}}}{\nu_{\text{FSR}}}\pi\right)\right]^{-1}, \tag{B1}$$

where L is the length of the cavity, and $\nu_{\text{FSR}} = c/2L$ is the free spectral range. Using this equation to analyze the TEM_{00} and $\text{TEM}_{01}/\text{TEM}_{10}$ modes in the white-light spectrum measured for the bare cavity, we estimate an effective radius of curvature of 61.0 ± 1.4 μm for a bare cavity length of 13.3 μm and a beam radius of 2.6 μm on the fiber mirror. The same beam diameter would correspond to a cavity length of 22 μm for a cavity containing a 10.5 μm diamond membrane, as the beam diverges less in the higher refractive index medium. Deviation from the radius of curvature extracted from a parabolic fit to our interferometry measurement ($R \approx 50 \pm 1$ μm) arises because the finite diameter mode samples a range of curvatures within the Gaussian dimple.

APPENDIX C: NUMERICAL CAVITY MODEL

We have developed a numerical model to calculate the fundamental Gaussian cavity mode for a half-symmetric cavity containing a diamond membrane bonded to the flat mirror. The model first solves for the Gaussian beam parameters (waist radius and position) in both the air and diamond sections assuming a curved diamond surface lying along the mode

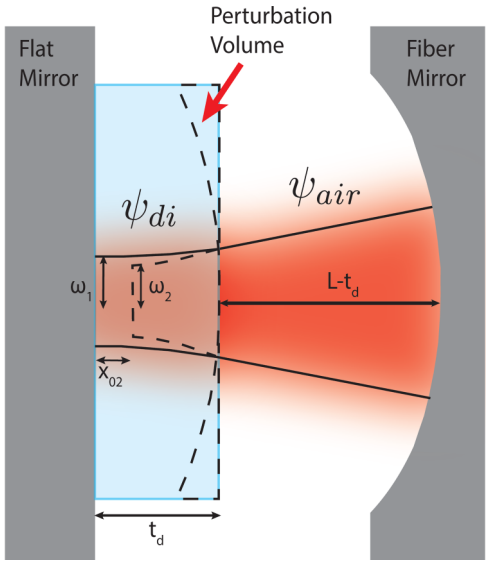

FIG. 6. (Color online) A diagram illustrating the $1/e^2$ intensity radius of the zero-order Gaussian modes in the diamond and air (solid lines). The mode in diamond has a waist with radius w_1 at the flat mirror, while the mode in air has a waist with radius w_2 a distance x_{02} from the mirror flat. The perturbation volume considered in Eq. (9) (dashed lines) is the difference between the presumed diamond interface lying along the mode wavefront and the planar diamond surface.

wavefront (see Fig. 6). As boundary conditions, we require that the beam diameters and radii of curvature are equal at the air-diamond interface to ensure electric field continuity. In addition, the radius of curvature in air should match the ablation radius of curvature at the fiber mirror, while the mode waist in diamond should lie at the flat mirror. With these four requirements, once can solve for the required radius of curvature for the air-diamond interface, the beam waists w_1 and w_2 corresponding to the modes in diamond and air, and the effective waist position x_{02} for the air mode.

Once the two Gaussian modes in the air and diamond regions are known, one can solve for the resonant frequencies and lengths of the cavity using transfer matrix theory applied to the left- and right-traveling electric fields within the cavity structure (see Fig. 7).

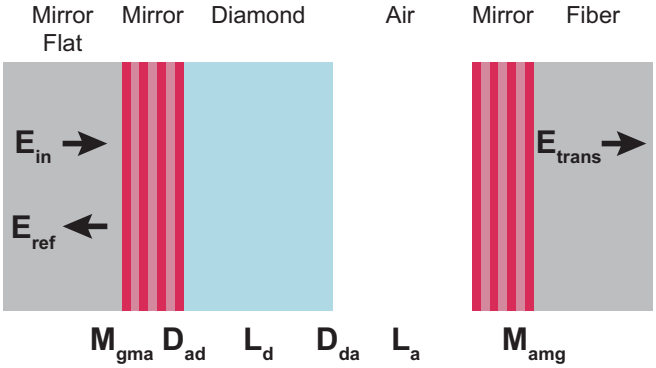

FIG. 7. (Color online) A diagram indicating the relevant transfer matrices used to calculate the resonant cavity frequencies and lengths.

Here, we model the full geometry of the flat mirror as a one-dimensional 29-layer dielectric stack where the right-moving electric field travels from glass into air; the transfer matrix describing this process is M_{gma}. Conversely, the fiber mirror is modeled as the inverse matrix ($M_{amg} = M_{gma}^{-1}$). Since the mirrors are defined for air termination, we need to include an additional matrix to model the air-diamond interface at the flat mirror (D_{ad}). As mentioned above, we assume that the second air-diamond interface (D_{da}) follows the curvature of the wavefronts at that position (dashed line in Fig. 6). The propagation matrices in the air and diamond include the Guoy phase, and they are given by

$$L_{\text{diamond}} = \begin{bmatrix} e^{-\frac{2\pi n_d}{\lambda} t_d + i\phi_1(t_d)} & 0 \\ 0 & e^{\frac{2\pi n_d}{\lambda} t_d - i\phi_1(t_d)} \end{bmatrix},$$

$$L_{\text{air}} = \begin{bmatrix} e^{-\frac{2\pi}{\lambda}(L-t_d)+i\phi_2(L-x_{02})} & 0 \\ 0 & e^{\frac{2\pi}{\lambda}(L-t_d)-i\phi_2(L-x_{02})} \end{bmatrix},$$

where $\phi_i(x) = \arctan(x\lambda/\pi w_i^2)$ is the Guoy phase, t_d is the diamond thickness, L is the cavity length, w_1 and w_2 are the $1/e^2$ radii at the diamond and air waists, respectively, and x_{02} is the effective beam waist position for the mode in air (see Fig. 6). The full transfer matrix for the cavity is

$$\begin{bmatrix} E_{\text{trans}} \\ 0 \end{bmatrix} = S \begin{bmatrix} E_{\text{in}} \\ E_{\text{ref}} \end{bmatrix}, \tag{C1}$$

where

$$S = M_{amg}\, L_a\, D_{da}\, L_d\, D_{ad}\, M_{gma}. \tag{C2}$$

Using the transmission curves calculated with this model, the linewidth in frequency and length can be determined. The field within the diamond and air regions can be found by evaluating subsets of the transfer matrices to find the amplitudes in the air and diamond, which are then multiplied by appropriate Gaussian modes.

When adding loss to this model, the dielectric indices used in the mirror stack and diamond were given small complex components; in addition, the interface matrices D_{da} and D_{ad} were modified according to Eqs. (4) and (5).

APPENDIX D: NONDEGENERATE PERTURBATION THEORY

The Hermite-Gaussian family of modes represents the eigenstates of a spherical resonator, satisfying the Helmholtz equation [47]. Introducing some small volume of material with a different refractive index can break the cavity symmetry, leading to a set of cavity eigenstates that can be expressed as a linear combination of the unperturbed cavity modes [41].

In our case, the zero-order modes correspond to solutions in the presence of a membrane whose interface is curved to follow a wavefront (see Fig. 6). They are defined by

$$\left[\nabla^2 + \kappa_i n_0^2(\mathbf{r})\right]\psi_i^0(\mathbf{r}) = 0, \tag{D1}$$

where ψ_i^0 are the zero-order modes of the system, $\kappa_i = (\frac{\omega_i}{c})^2$ contains the corresponding eigenfrequencies ω_i, and $n_0^2(\mathbf{r})$ is the index of refraction inside the cavity assuming an air-diamond interface following the mode wavefront. These zero-order eigenfunctions may be found exactly as a (real-valued) Hermite-Gaussian family of modes with different parameters in the air and diamond regions (see Appendix C). The orthonormalization condition is

$$\iiint \psi_m^0(\mathbf{r}) n_0^2(\mathbf{r}) \psi_n^0(\mathbf{r}) d^3\mathbf{r} = \delta_{mn}, \tag{D2}$$

where δ_{mn} is the Kronecker delta, the integral is taken over the cavity volume, and subscripts m and n encode all transverse and longitudinal mode indices.

We wish to calculate the perturbative effect of the membrane planarity, which is equivalent to introducing a small piece of dielectric representing the difference between the curved surface and a flat one. We are interested in a fundamental transverse mode (which is nondegenerate), for which the exact eigenstate ψ satisfies

$$\left\{\nabla^2 + \kappa\left[n_0^2(\mathbf{r}) + \lambda\mathcal{V}(\mathbf{r})\right]\right\}\psi = 0, \tag{D3}$$

where $\mathcal{V}(\mathbf{r}) = n_d^2 - 1$ inside the perturbation volume (and zero outside), λ is some small number, and κ corresponds to the new eigenfrequency. We can express both ψ and κ as a power series in λ:

$$\psi = \psi_0^0 + \sum_{n=1}^{\infty} \lambda^n \psi^n, \tag{D4}$$

$$\kappa = \kappa_0 + \sum_{n=1}^{\infty} \lambda^n \Delta_n, \tag{D5}$$

where ψ_0^0 and κ_0 correspond to the nondegenerate fundamental mode eigenstate of the unperturbed system, and ψ^n, Δ_n are the nth-order corrections. Considering only the terms of Eq. (D3) to order λ, one finds

$$\left[\nabla^2 + n_0^2(\mathbf{r})\kappa_0\right]\psi^1 = -\left[\Delta_1 n_0^2(\mathbf{r}) + \kappa_0\mathcal{V}(\mathbf{r})\right]\psi_0^0, \tag{D6}$$

and one can thereby derive the first-order correction to the eigenstate:

$$\psi^1 = \kappa_0 \sum_{m\neq 0} \frac{\iiint \psi_m^0(\mathbf{r})\mathcal{V}(\mathbf{r})\psi_0^0(\mathbf{r}) d\mathbf{r}^3}{\kappa_m - \kappa_0}\psi_m^0, \tag{D7}$$

where ψ_m^0 is the mth-order mode of the unperturbed system, and we have set $\lambda = 1$. Here m labels all longitudinal and transverse modes to which the zero-order Gaussian mode ψ_0^0 can be coupled by the perturbation.

[1] M. Lončar and A. Faraon, MRS Bull. **38**, 144 (2013).

[2] I. Aharonovich and E. Neu, Adv. Opt. Mater. **2**, 911 (2014).

[3] R. Schirhagl, K. Chang, M. Loretz, and C. L. Degen, Ann. Rev. Phys. Chem. **65**, 83 (2014).

[4] L. Rondin, J. Tetienne, T. Hingant, J. Roch, P. Maletinsky, and V. Jacques, Rep. Prog. Phys. **77**, 056503 (2014).

[5] T. D. Ladd, F. Jelezko, R. Laflamme, Y. Nakamura, C. Monroe, and J. L. O'Brien, Nature (London) **464**, 45 (2010).

[6] K. Nemoto, M. Trupke, S. J. Devitt, A. M. Stephens, B. Scharfenberger, K. Buczak, T. Nöbauer, M. S. Everitt, J. Schmiedmayer, and W. J. Munro, Phys. Rev. X **4**, 031022 (2014).

[7] M. W. Doherty, N. B. Manson, P. Delaney, F. Jelezko, J. Wrachtrup, and L. C. Hollenberg, Phys. Rep. **528**, 1 (2013).

[8] M. J. Burek, Y. Chu, M. S. Z. Liddy, P. Patel, J. Rochman, S. Meesala, W. Hong, Q. Quan, M. D. Lukin, and M. Lončar, Nat. Commun. **5**, 5718 (2014).

[9] B. Khanaliloo, M. Mitchell, A. C. Hryciw, and P. E. Barclay, Nano Lett. **15**, 5131 (2015).

[10] J. C. Lee, D. O. Bracher, S. Cui, K. Ohno, C. A. McLellan, X. Zhang, P. Andrich, B. Alemán, K. J. Russell, A. P. Magyar *et al.*, Appl. Phys. Lett. **105**, 261101 (2014).

[11] A. Faraon, C. Santori, Z. Huang, V. M. Acosta, and R. G. Beausoleil, Phys. Rev. Lett. **109**, 033604 (2012).

[12] D. Hunger, T. Steinmetz, Y. Colombe, C. Deutsch, T. W. Hänsch, and J. Reichel, New J. Phys. **12**, 065038 (2010).

[13] A. Muller, E. B. Flagg, J. R. Lawall, and G. S. Solomon, Opt. Lett. **35**, 2293 (2010).

[14] H. Kaupp, C. Deutsch, H.-C. Chang, J. Reichel, T. W. Hänsch, and D. Hunger, Phys. Rev. A **88**, 053812 (2013).

[15] R. Albrecht, A. Bommer, C. Deutsch, J. Reichel, and C. Becher, Phys. Rev. Lett. **110**, 243602 (2013).

[16] R. Albrecht, A. Bommer, C. Pauly, F. Mücklich, A. W. Schell, P. Engel, T. Schröder, O. Benson, J. Reichel, and C. Becher, Appl. Phys. Lett. **105**, 073113 (2014).

[17] S. Johnson, P. Dolan, T. Grange, A. Trichet, G. Hornecker, Y. Chen, L. Weng, G. Hughes, A. Auffèves, and J. Smith, arXiv:1506.05161v2.

[18] C. Santori, P. Barclay, K. C. Fu, R. Beausoleil, S. Spillane, and M. Fisch, Nanotechnology **21**, 274008 (2010).

[19] P. Tamarat, T. Gaebel, J. Rabeau, M. Khan, A. Greentree, H. Wilson, L. Hollenberg, S. Prawer, P. Hemmer, F. Jelezko *et al.*, Phys. Rev. Lett. **97**, 083002 (2006).

[20] Y. Chu, N. P. de Leon, B. J. Shields, B. Hausmann, R. Evans, E. Togan, M. J. Burek, M. Markham, A. Stacey, A. S. Zibrov, A. Yacoby, D. J. Twitchen, M. Lončar, H. Park, P. Maletinsky, and M. D. Lukin, Nano Lett. **14**, 1982 (2014).

[21] S. L. Mouradian, T. Schröder, C. B. Poitras, L. Li, J. Goldstein, E. H. Chen, M. Walsh, J. Cardenas, M. L. Markham, D. J. Twitchen, M. Lipson, and D. Englund, Phys. Rev. X **5**, 031009 (2015).

[22] J. Miguel-Sánchez, A. Reinhard, E. Togan, T. Volz, A. Imamoglu, B. Besga, J. Reichel, and J. Estève, New J. Phys. **15**, 045002 (2013).

[23] C. Toninelli, Y. Delley, T. Stöferle, A. Renn, S. Götzinger, and V. Sandoghdar, Appl. Phys. Lett. **97**, 021107 (2010).

[24] D. Hunger, C. Deutsch, R. J. Barbour, R. J. Warburton, and J. Reichel, AIP Adv. **2**, 012119 (2012).

[25] B. Brandstätter, A. McClung, K. Schüppert, B. Casabone, K. Friebe, A. Stute, P. O. Schmidt, C. Deutsch, J. Reichel, R. Blatt, and T. E. Northup, Rev. Sci. Instrum. **84**, 123104 (2013).

[26] B. J. M. Hausmann, B. Shields, Q. Quan, P. Maletinsky, M. McCutcheon, J. T. Choy, T. M. Babinec, A. Kubanek, A. Yacoby, M. D. Lukin, and M. Lončar, Nano Lett. **12**, 1578 (2012).

[27] Y. Tao and C. Degen, Adv. Mater. **25**, 3962 (2013).

[28] P. Ovartchaiyapong, L. M. A. Pascal, B. A. Myers, P. Lauria, and A. C. Bleszynski Jayich, Appl. Phys. Lett. **101**, 163505 (2012).

[29] D. Freedman and P. Diaconis, Z. Wahrschein. Verwandt. Geb. **57**, 453 (1981).

[30] A. M. Jayich, J. C. Sankey, B. M. Zwickl, C. Yang, J. D. Thompson, S. M. Girvin, A. A. Clerk, F. Marquardt, and J. G. E. Harris, New J. Phys. **10**, 095008 (2008).

[31] A significantly more complicated analytic expression including the Guoy phase and transverse mode profile was also derived, but due to the equation complexity and other systematic measurement errors (including stage drift and nonlinearity), the latter model did not improve precision of the membrane thickness and cavity length estimates.

[32] The increased uncertainty arises because the LED used to obtain the white-light spectrum heats the cavity, and we must allow it to attain thermal equilibrium before acquiring data. We track length changes as the structure warms, but we can only calibrate them within $\sim \pm \lambda/4$.

[33] White-light spectra were taken at each membrane region, but the variation in thickness was below our measurement precision of $\sim$200 nm, illustrating that even slight changes in diamond thickness can drastically change the finesse measured for a given laser frequency.

[34] J. Szczyrbowski and A. Czapla, Thin Solid Films **46**, 127 (1977).

[35] C. C. Katsidis and D. I. Siapkas, Appl. Opt. **41**, 3978 (2002).

[36] L. C. Bassett, F. J. Heremans, C. G. Yale, B. B. Buckley, and D. D. Awschalom, Phys. Rev. Lett. **107**, 266403 (2011).

[37] J.-M. Gerard, in *Single Quantum Dots* (Springer, Berlin, 2003), Vol. 90, pp. 269–314.

[38] C. Sauvan, J. P. Hugonin, I. S. Maksymov, and P. Lalanne, Phys. Rev. Lett. **110**, 237401 (2013).

[39] D. J. Wilson, C. A. Regal, S. B. Papp, and H. J. Kimble, Phys. Rev. Lett. **103**, 207204 (2009).

[40] W. Joyce and B. DeLoach, Appl. Opt. **23**, 4187 (1984).

[41] I. Favero, J. Sankey, and E. Weig, in *Cavity Optomechanics*, Quantum Science and Technology, edited by M. Aspelmeyer, T. J. Kippenberg, and F. Marquardt (Springer, Berlin, 2014), pp. 83–119.

[42] J. Benedikter, T. Hümmer, M. Mader, B. Schlederer, J. Reichel, T. W. Hänsch, and D. Hunger, New J. Phys. **17**, 053051 (2015).

[43] D. Kleckner, W. T. M. Irvine, S. S. R. Oemrawsingh, and D. Bouwmeester, Phys. Rev. A **81**, 043814 (2010).

[44] H. Bernien, B. Hensen, W. Pfaff, G. Koolstra, M. S. Blok, L. Robledo, T. H. Taminiau, M. Markham, D. J. Twitchen, L. Childress, and R. Hanson, Nature (London) **497**, 86 (2013).

[45] J. Gallego, S. Ghosh, S. K. Alavi, W. Alt, M. Martinez-Dorantes, D. Meschede, and L. Ratschbacher, arXiv:1508.05289.

[46] A. Bick, C. Staarmann, P. Christoph, O. Hellmig, J. Heinze, K. Sengstock, and C. Becker, arXiv:1508.06521.

[47] B. E. Saleh, M. C. Teich, and B. E. Saleh, *Fundamentals of Photonics* (Wiley, New York, 1991), Vol. 22.